INTERNATIONAL JOURNAL FOR NUMERICAL METHODS IN FLUIDS
Int. J. Numer. Meth. Fluids 2002; **38**:747–768 (DOI: 10.1002/fld.247)

Finite volume scheme for the solution of fluid flow problems on unstructured non-staggered grids

I. E. Barton[1], D. Markham-Smith[1,*] and N. Bressloff[2]

[1]*Department of Mechanical Engineering, Brunel University, Uxbridge, Middlesex, UB8 3PH, U.K.*
[2]*School of Engineering Sciences, Department of Mechanical Engineering, University of Southampton, Highfield, Southampton SO17 1BJ, U.K.*

SUMMARY

A recently developed non-staggered methodology which uses the principle of applying fourth-order dissipation to the governing pressure-correction equation is developed so it can be applied to unstructured grids. A finite volume methodology is used for discretization. The fourth-order dissipation term is found using second-order gradient operators. This makes it straightforward to incorporate the dissipation term on unstructured grids. The new methodology is compared with solutions from a standard finite volume second-order flow solver and is also tested for a standard laminar driven-lid flow problem with grids systems that do not have a uniform structure. Finally, we demonstrate how the new methodology can be used to predict flow over a wavy boundary. Copyright © 2002 John Wiley & Sons, Ltd.

KEY WORDS: non-staggered methodology; finite volume; unstructured grids; wavy boundary

1. INTRODUCTION

In this paper a new non-staggered grid methodology for the solution of fluid flows on unstructured grids is developed and compared with a Navier–Stokes solver developed by Bressloff [1], using the SIMPLEC technique, finite volume scheme and second-order upwind differencing. The methodology combines techniques employed in the meshless methods [2] and uses artificial diffusion applied in the flow direction on the non-staggered (co-located) grid with fourth-order pressure dissipation. The methodology therefore has several unusual features, combining to form a novel methodology. First we will concentrate on the non-staggered features of the presented scheme.

In principle, non-staggered methodologies have many advantages. However, staggered methodologies have the implicit advantage that odd–even coupling is prevented [3]. A popular non-staggered scheme employs the technique of 'momentum interpolation' in order to cure the problem of odd–even coupling. This scheme has first proposed by Rhie and Chow [4] and has been used by several other investigators [5–7]. The Rhie and Chow scheme is the

*Correspondence to: D. Markham-Smith, Mechanical Engineering Department, Brunel University, Uxbridge, Middlesex, UB8 3PH, U.K.

Received 8 December 1998
Revised 6 August 2001

methodology that we propose to develop. We will not dwell on the advantages of developing this or any other non-staggered methodology, they have been detailed elsewhere [8]. However, one important benefit is it can simplify the overall numerical coding. On the whole, this important benefit is lost using the non-staggered methodology developed by Rhie and Chow [4] when applied to unstructured grids, although, the Rhie and Chow method is relatively straightforward to apply to Cartesian grids. Armfield has adapted the original Rhie and Chow method for this express purpose [9, 10]. It is also true to state that developing Rhie and Chow's method for non-Cartesian grids presents little difficulties provided body-fitted coordinates are used owing to the fact that there is a regular mapping of nodes and regular 'differences' between nodes. Whereas an unstructured grid poses a greater difficulty for the Rhie and Chow method because these conditions do not apply, any advantages in terms of simplifying the code are lost. We believe that this can be avoided if a pressure dissaption technique is employed [11]. Thus the new methodology follows the principle of the Rhie and Chow method but employs alternative numerical analysis. We briefly outline the non-staggered methodology, described in more detail by Barton and Kirby [12].

2. THE NEW METHODOLOGY

2.1. The pressure dissipation

In part, this paper is a direct continuation of Reference [12] which developed a non-staggered methodology for Cartesian grid problems. The main difference relates to the integration of the governing equations around control volumes. The solution of the governing equation is based on the standard SIMPLE algorithm [3]. The algorithm calculates the pressure field by ensuring mass-continuity is satisfied. This requirement causes a major difficulty when implementing non-staggered methodologies, because continuity cannot be integrated directly around a single pressure node without interpolation. Another way to describe this difficulty is to say that an individual velocity node is not directly linked to its pressure gradient. The argument proposed in Reference [4] to avoid this problem is that the cell-face velocities require special interpolation introducing an additional term similar to fourth-order dissipation being applied to the governing pressure-correction equation. Rhie and Chow introduce the dissipation term 'indirectly' or, arguably, in a 'disguised format'. However, Armfield [9, 10] has modelled problems by directly applying this term to the governing pressure-correction equation. The difficulty dealing with the dissipation term presented by Armfield is it is far from straightforward how to apply it to an unstructured grid. We can avoid this problem by constructing the fourth-order pressure dissipation term from a repeated application of second-order operators, e.g.

$$\frac{\mathrm{d}^4 p}{\mathrm{d}x^4} \approx \nabla_x^2 \nabla_x^2 p \tag{1}$$

Unlike a (directly constructed) fourth-order operator, it is straightforward to construct a second-order operator (that is second-order accurate) because it only requires the central node and its surrounding nodes that form the computational molecule. In essence then, the first step is to find a field-variable constructed from $\nabla_x^2 p$ and then re-apply the operator to find

the dissipation term. Adiabatic conditions are employed for the second step in order to avoid continuity leaking out of the boundaries.

The 'exact' dissipation term that Rhie and Chow introduce into the governing pressure-correction equation can be expressed as

$$ {}_{2\delta}\nabla_x \frac{1}{B^u}\, {}_{2\delta}\nabla_x p - {}_{1\delta}\nabla_x \frac{1}{B^u}\, {}_{1\delta}\nabla_x p \tag{2} $$

for the x-co-ordinate on a Cartesian grid. The B coefficients are the pole-coefficients used in the algebraic governing velocity equations. The exact dissipation term is the difference of the divergence of the pressure gradients over two-nodal spacings compared with one-nodal spacing. In Reference [12] it is assumed that the B coefficients can be considered to be slowly varying in comparison with variation of the pressure field and therefore we can use the following approximation:

$$ \text{If} \quad \frac{\partial^2 \phi}{\partial x^2} = \nabla^2 \phi = \sum_M A_M^{xx} (\phi_M - \phi_p) $$

$$ \text{Let} \quad \frac{\partial}{\partial x} \frac{1}{\gamma} \frac{\partial \phi}{\partial x} = \sum_M A_M^{xx} \left(\frac{\gamma_M + \gamma_P}{2} \right) (\phi_M - \phi_p) \tag{3} $$

where M refers to the surrounding nodes and ϕ_p is the pole node. A is an algebraic coefficient. The double 'xx' superscript refers to the fact that it is a second-order differential in the x-direction and the γ is a general flow property for the example, we may wish to use $(\partial/\partial x)\mu(\partial/\partial x)u$. The methodology can now take advantage of the fact that we can make the following approximation:

$$ \frac{{}_{2\delta}\nabla^2}{B^u} p - \frac{{}_{1\delta}\nabla^2}{B^u} p \cong \left(\frac{\Delta x^2}{4} \right) \frac{{}_{1\delta}\nabla^4}{B^u} p \tag{4} $$

The right-hand term is in the form of a fourth-order operator which acts as a smoothing term for the pressure field. The only problem with the implementation of this operator term is that it is multiplied by a squared unit-length. To remove this length scale we introduce a special second-order operator $\vee^2$. This term is defined as follows:

$$ \text{Let} \quad \vee^2 \phi = \sum_M A_M^{xx} (\phi_M - \phi_O)/A_O $$

$$ \text{where} \quad A_O = \sum_M A_M^{xx} \tag{5} $$

By introducing this operator we have the pressure dissipation term with the correct dimensions. A further discussion of this operator is presented in Reference [11]. Referring back to Equation (1), the operator $\vee^2$ can be used as the first-step in order to the find the fourth-order dissipation term. The operator ∇^2/γ expressed in Equation (3) can be used as the second-step. In summary, we use a pressure dissipation term in the form

$$ \text{dissipation} = \alpha \left(\frac{\nabla_x^2}{B^{ug}} \vee_x^2 p + \frac{\nabla_y^2}{B^{vg}} \vee_y^2 p \right) \tag{6} $$

The amount of applied dissipation needs to be minimized as excessive application we have found causes a detrimental effect on the overall results. In the simulations presented we set $\alpha = 0.04$. In comparison with the Rhie and Chow method, their value of $\propto$ is equivalent to 0.5. The value used in the current methodology is much lower because the above dissipation term uses B^{g} coefficients, (the g superscript refers to geometrical terms). The B^{g} coefficients only contain the geometrical discretized terms and it excludes temporal and pseudo-temporal terms. Meaning that the dissipation term is not dependent on the time-step or under-relaxation. This error was over-looked in Rhie and Chow's original methodology as pointed out in References [13, 14].

The methodology we have presented is similar to that in Reference [12], the main difference concerns how the terms are discretized. This includes, of course, how we generate the operators ∇^2 and $\vee^2$ give this step is straightforward, the current methodology can be easily developed for unstructured grids.

2.2. *The meshless methodology discretization*

The current work was developed as part of a meshless methods solver applied to a finite volume grid system. Modifying a meshless method solver and its discretization approach for dealing with a finite volume grid system has been independently developed [15]. We can fit spatial functions or apply the Gauss Law to find the coefficients associated with derivative terms, (or, in our case, derivative terms that are integrated across the control volume).

We use a control volume approach in order to generate the derivative terms such as $\partial\phi/\partial x$ and $\partial^2\phi/\partial x^2$. A control volume is illustrated in Figure 1. The central node is located at the centre of the computational molecule. The control volume for the second-derivatives is formed by connecting adjacent centroids. The divergence theorem is applied to obtain the first derivative

$$\frac{\partial\bar{\phi}}{\partial x} = \frac{1}{A_{\mathrm{CV}}} \iint_{\mathrm{CV}} \frac{\partial\phi}{\partial x}\,\mathrm{d}x\,\mathrm{d}y = \frac{1}{A_{\mathrm{CV}}} \oint_{\mathrm{CV}} \phi\underline{i} \times \mathrm{d}\underline{s}$$

$$\approx \frac{1}{A_{\mathrm{CV}}} \sum_{M} \left(\frac{\phi_M + \phi_{M+1}}{2} \right) \Delta y_{M \to M+1} \tag{7}$$

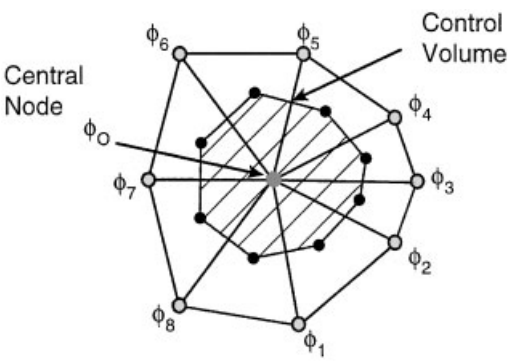

Figure 1. Illustration of a computational molecule and its control volume structure.

where A_{CV} is the area of the control volume. The discretization procedure collects ϕ_M terms and then stores them so the final discretized term is in a finite-element format where the operator can be expressed as

$$\frac{\partial \bar{\phi}}{\partial x} \approx \sum_M A_M^x (\phi_M - \phi_O) \tag{8}$$

A similar (more complex) procedure is applied to obtain the second-derivative terms, $\partial^2\phi/\partial x^2$. In this case the problem needs to be broken into two parts. The first part is to integrate around a small triangle to find the first-order derivative at the centroid. Consider a Mth triangle:

$$\begin{aligned}\left(\frac{\partial \bar{\phi}}{\partial x}\right)_M &= \frac{1}{A_M}\iint_M \frac{\partial \phi}{\partial x}\,\mathrm{d}x\,\mathrm{d}y = \frac{1}{A_M}\oint_M \phi \underline{i}\,\mathrm{d}\underline{s} \\ &\approx \frac{1}{2A_M}[(\phi_O + \phi_M)\Delta y_{O\to M} + (\phi_M + \phi_{M+1})\,\Delta y_{M\to M+1} \\ &\quad + (\phi_{M+1} + \phi_O)\,\Delta y_{M+1\to O}]\end{aligned} \tag{9}$$

The final result is formed by using the substitution of the $(\partial\phi/\partial x)_M$ terms into the following expression:

$$\begin{aligned}\frac{\partial^2 \bar{\phi}}{\partial x^2} &= \frac{1}{A_{CV}}\iint_{CV} \frac{\partial^2 \phi}{\partial x^2}\,\mathrm{d}x\,\mathrm{d}y = \frac{1}{A_{CV}}\oint_{CV}\left(\frac{\partial \bar{\phi}}{\partial x}\right)_M \underline{i} \times \mathrm{d}\underline{s} \\ &\approx \frac{1}{2A_{CV}}\sum_M \left(\left(\frac{\partial \bar{\phi}}{\partial x}\right)_M + \left(\frac{\partial \bar{\phi}}{\partial x}\right)_{M+1}\right)\Delta y^c_{M\to M+1}\end{aligned} \tag{10}$$

The superscript 'c' denotes that we now integrate form one centroid position to the next. By collecting the various coefficients together we can then obtain the final result in the form:

$$\frac{\partial^2 \bar{\phi}}{\partial x^2} \approx \sum_M A_M^{xx}(\phi_M - \phi_o) \tag{11}$$

The discretization of the governing equations is now straightforward because we have established the discretized partial-derivative operators. These operators are merely substituted for the partial derivatives found in the governing equations in order to obtain the governing algebraic equations. The governing equations used in the SIMPLE scheme are Navier–Stokes equations (linearized with respect to time); a velocity correction equation and a pressure correction equation. One of the advantages of using a non-staggered grid methodology is that the same operators are used for the velocity governing equations and the pressure governing equation. Finally, we will consider the treatment of the governing pressure-correction equation, in partial derivatives this is expressed as

$$0 = \frac{\partial u^*}{\partial x} + \frac{\partial v^*}{\partial y} - \left(\frac{\partial}{\partial x}\frac{1}{B^u}\frac{\partial p'}{\partial x} + \frac{\partial}{\partial y}\frac{1}{B^v}\frac{\partial p'}{\partial y}\right) + \text{dissipation} \tag{12}$$

where u^*, v^* denote the intermediate velocity field calculations and p' is the velocity field calculations and p' is the pressure correction used in the SIMPLE algorithm. The equation contains an 'intermediate' continuity term; a Laplacian-type operator for the pressure-correction and the pressure dissipation term. Integrating the second term in two-steps means an expanded computational molecule is formed (a problem associated with using a non-staggered grid). Since we encountered this difficulty before with Equation (2), we use the same approximation expressed in Equation (3) to deal with this term.

2.3. *Differencing scheme*

The technique proposed in Reference [2] uses a novel method to discretise the nodal grid produced. We aspire to make a flexible, versatile and robust solution. In order to prevent oscillations in the spatial solution of the results during the repeated use of the solver a system is used to add artificial viscosity (v), also known as numerical dissipation (extra diffusion). This equivalent to dampening the system of equations. When discretised the spatial polynomial does not implicitly contain enough artificial viscosity so invariably the solution becomes unstable. Therefore, it is necessary to explicitly add an amount to stabilize the solution. The disadvantage of applying artifical viscosity is that it compromises the accuracy of the solution, it also has a further problem of reducing the hyperbolic nature of the equations causing slower convergence.

In previous methodologies a polynomial is applied with a basis in the x and y. As the flow direction is not considered no weighting factors influence the variables in the flow direction. In order to achieve a basis of the flow therefore it is proposed that a new co-ordinate system (ε, η) based on flow direction should be applied. This will allow the artificial viscosity to be applied to the flow direction only and not to any other plane.

At present the spatial polynomial applied for a four-node relationship is as follows:

$$\phi = a_0 + a_1 x + a_2 x^2 + a_3 y + a_4 y^2 \tag{13}$$

The transformation to change co-ordinates from $\Phi(x, y)$ to $\Phi(\varepsilon, \eta)$ is

$$\begin{pmatrix} \varepsilon \\ \eta \end{pmatrix} = \begin{pmatrix} \cos\theta & \sin\theta \\ -\sin\theta & \cos\theta \end{pmatrix} \begin{pmatrix} x \\ y \end{pmatrix} \tag{14}$$

Now the general transport equation for u or v can be represented by

$$\frac{\partial \rho \varepsilon' \phi}{\partial \varepsilon} + \frac{\partial \rho \eta' \phi}{\partial \eta} = \left(\frac{\partial^2 \phi}{\partial \varepsilon^2} + \frac{\partial^2 \phi}{\partial \eta^2} \right) + S_{\varepsilon\eta} \tag{15}$$

In summary, the proposed transformed co-ordinate system allows more discrete and more effective use of artificial viscosity with its application in the flow direction during a solution. Due to which the solution is numerically stable in the flow direction with the application of artificial viscosity and the solution should be more hyperbolic in comparison with a scheme that independently test for numerical stability in the x and y directions.

2.4. *Matrix solver*

Various matrix solvers were tried including TDMA (tri-diagonal matrix algorithm), Guass–Seidel and Conqurate conjugate gradient methods. A simple Guass–Seidel solver was found to

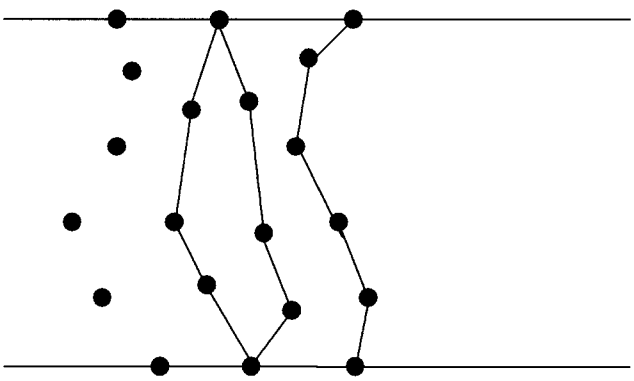

Figure 2. Illustration of boundary elements that are used to calculate the boundary pressures.

be effective for solving the velocity field whereas the pressure field was solved most effectively using a modified TDMA solver for a non-regular grid system. The lines within the modified TDMA are constructed to ensure every node in non-uniform grids are solved, an illustration of three constructed lines are shown in Figure 2. A normal TDMA solver is detailed in Reference [16]. The algorithm sweeps through the solution domain until the residuals reduce by four orders of magnitude.

Typically, results are considered to have converged if residuals reduce by at least four orders of magnitude. The methodology applies the following boundary conditions. First-order upwind interpolation is applied at the outlet boundary. Inlet velocity values are prescribed. No-slip boundary conditions are applied at the walls. Second-order extrapolation is applied for the pressure field. Pressure at the boundaries are calculated using extrapolation over three points which are located on the intersect of a line normal to the boundary. This is illustrated in Figure 3. For wall pressure nodes the condition that $\partial p/\partial n = 0$ is incorporated into the extrapolation.

3. THE FINITE VOLUME METHODOLOGY

A finite volume solver developed at Southampton University [1] was used to test for grid-independent solutions to two standard numerical test cases; flow through a sudden expansion and flow past a cylinder. The standard solver employs a multi-block method for structured grids [19] and the SIMPLEC (semi-implicit pressure linked equations consistent) [18] pressure correction technique as its solution algorithm. The well established technique of using momentum interpolation [13] is used (for the evaluation of control volume face fluxes) to avoid pressure–velocity decoupling. Convection fluxes are discretized using deferred correction [19] and Van Leer's high resolution curved line advection method (CLAM) [20] and diffusion fluxes are approximated by central differences.

Although the new methodology can be used with any type of grid system, for comparison purposes, it is tested grids for two problems generated for the standard finite volume solver. For the backstep problem, two blocks are used; one upstream and one downstream of the expansion and two blocks are also used to mesh the cylinder problem, one on each side of

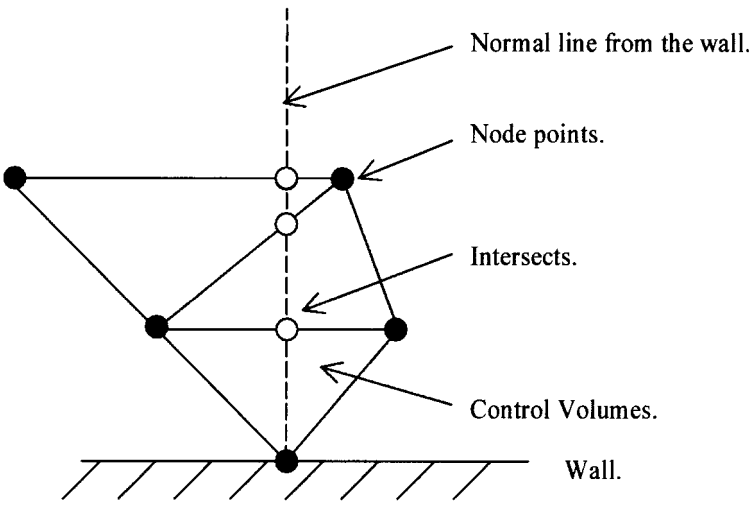

Figure 3. Illustration of the construction of the matrix data point around the calculation node.

the centre-line drawn parallel to the solid walls. Whereas the backstep geometry can be solved on a Cartesian grid, the cylinder geometry demands a curvilinear solver. Contravariant vectors are employed in the momentum interpolation procedure and Cartesian velocity components are used as dependent variables in the momentum equations [21, 22]. Further details of the standard scheme are discussed [1].

4. EXAMPLE APPLICATIONS

The new methodology was tested with comparisons against the finite volume solver simulations for flow over a backward facing step and flow around a circular cylinder. After good agreement was achieved between the two methodologies, the problem of laminar flow in a square cavity with a driven lid was examined for the new methodology, and we show simulations of laminar flow over a wavy boundary.

4.1. Flow over a backward facing step

Flow over a backward facing step has important fluid dynamic features, which are caused by the instantaneous change of dimensions within the system. These flow features can be observed in numerous engineering applications. For a closed duct flow there is an upper re-circulation area, which causes the growth of the lower attachment point to be decreased. The upper separation is caused by an adverse pressure gradient while pressure recovery causes the upper reattachment [23].

Experimental work, by Armaly *et al.* [24], has formed the backbone of many comparative studies. Their findings are of major importance within the field, despite the fact that the agreement between the numerical analysis and the experimental was only acceptable up to Reynolds number of 500 due to numerical diffusion. There are many numerical simulations

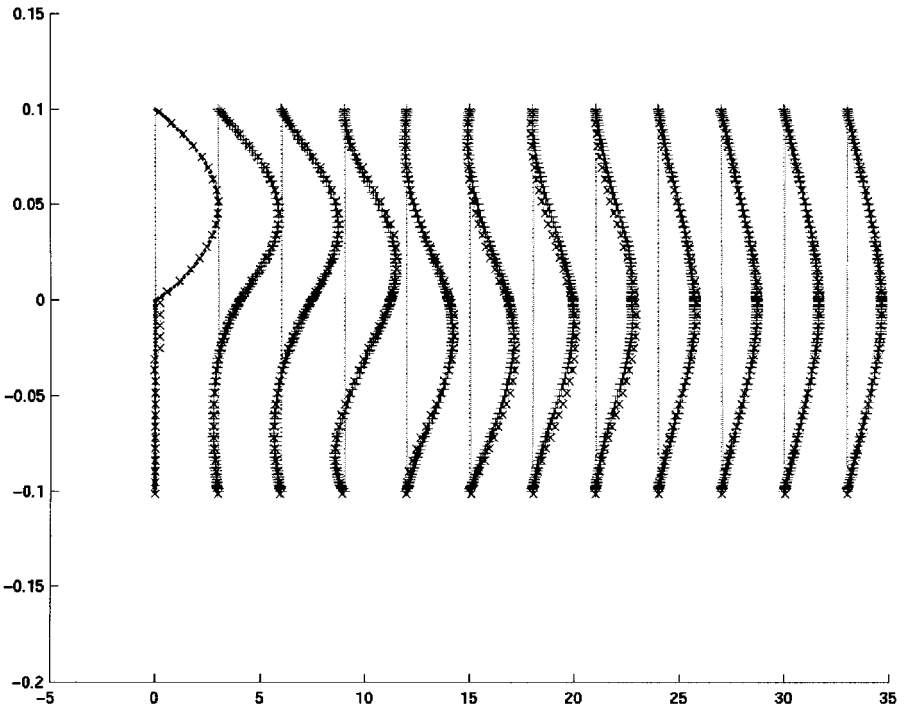

Figure 4. Comparison of the flow over a backward facing step with the Navier–Stokes solver represented by the + and the non-staggered methodology represented by the ×.

[25–29], where good agreement in two dimensions has been recorded, more recent studies have also considered three-dimensional effects [30].

It is straightforward to develop grid independency tests as grid resolution has been examined by a number of authors such as [31, 32]. While the work of [27] specifically considered a non-uniform grid distribution. Other studies have looked at specific areas, for example [33, 6] studied the behaviour of boundary conditions. This work allows us to make a numerical assessment of the required grid refinement.

Figure 4 shows a comparison of the u velocity profiles over the backward facing step for two different methodologies, the standard finite volume solver and the new methodology. Both simulations were generated for a Reynolds number of 800, the length scale was based on two inlet heights, the standard solver profiles were generated on a Cartesian with 7500 nodes and the non-staggered grid methodology used a similar grid of 10,000 nodes. The new methodology was run over 3000 iterations, which were required to achieve a convergence criteria of 4 orders of magnitude. The profiles for the two methodologies are virtually identical. Note the testing of the new methodology used various grid distributions, shown in grids 1, 3 and 5. The results shown for the new methodology are grid independent. As excepted a finer grid is required, in comparison with a scheme that uses second-order upwind differencing.

Figure 5 shows results for a 50×50 non-staggered grid and how the results are improved with a finer 100×100 grid in comparison with the standard solver.

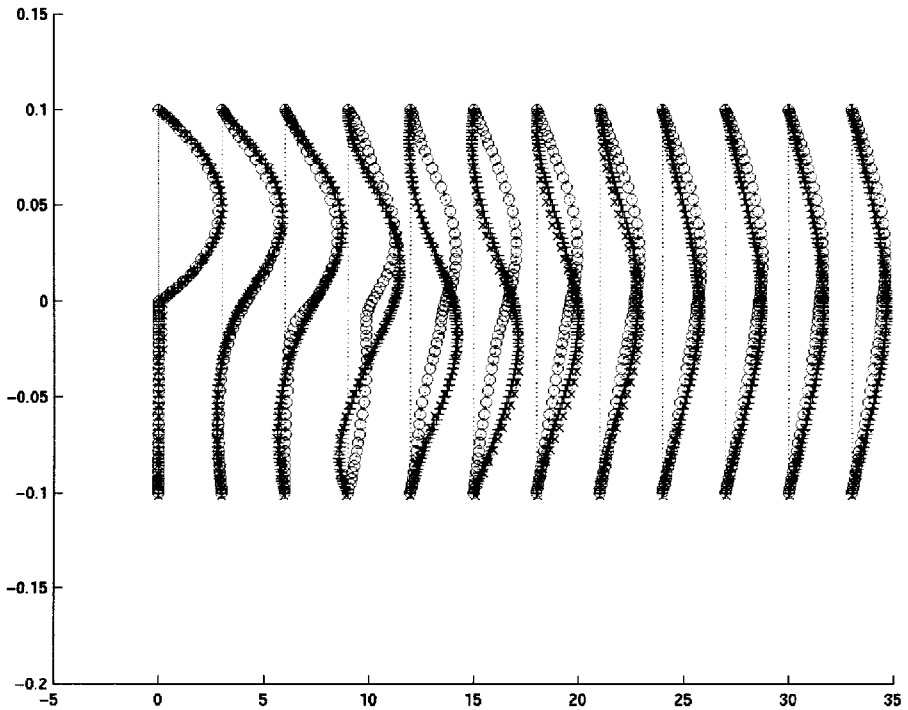

Figure 5. Comparison of results produced by the Navier–Stokes solver, ×, the non-staggered methodology run on a 100×100 grid + and the non-staggered methodology run on a 50×50 grid ○.

4.2. Flow around a circular cylinder

Similar to the flow over a backward facing step we show a *u*-velocity profile comparison in Figure 6 for flow around a circular cylinder produced by the two different methodologies on the same grid system. The Reynolds number was set to 25 to avoid instability and the lower and top walls were set to zero-velocity. Unlike the comparison made for the flow over the backward facing step there are obvious discrepancies though the general velocity profiles are very similar. Unfortunately, we are approaching an upper CPU memory requirement, computer spec PII with a 128 M of RAM, we have not been able to confirm if the new methodology has achieved grid independence.

4.3. Driven-lid flow

The methodology is now assessed using the popular numerical problem for laminar flow in a square cavity with a driven lid. It is a typical test used for non-staggered methodologies, (see for example References [34–36]). The problem is illustrated in Figure 7. The illustration shows a large vortex in the middle of a square cavity which is created by a 'driven-lid'. A fine grid (80×80) is used as a datum set of results. The predictions using the fine grid are solved using the scheme presented in Reference [12], which is a finite difference method for uniform Cartesian grid systems. The new methodology is applied to five different 20×20

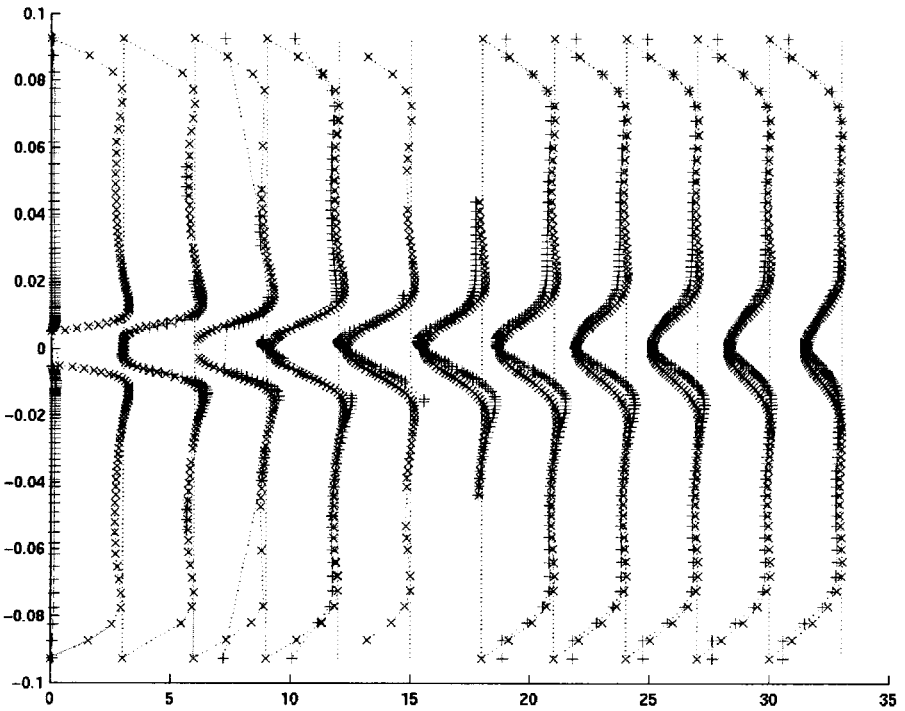

Figure 6. Comparison of the flow over a cylinder between the Navier–Stokes solver represented by the + and the nonstaggered methodology represented by the ×.

grids. Discussion focuses on grids 1, 3 and 5, although results 2 and 4 are not discussed in the paper, they helped to establish linear trends. Grid 1 is a regularly-spaced triangular grid system and grids 2–5 are increasingly deformed versions of grid 1. The deformed grids 1, 3 and 5 are shown in Figure 8. Each grid system has an unchanged central line of grid points allow you to make direct profile comparisons without the need for interpolation. The deformed grids have node points randomly displaced from their original position in the x and y directions within an increasing spatial range. The displaced nodes are randomly selected, where the probability of a displaced node increases with grid type. Grid 2 has a 20% chance for a displaced node, Grid 3 has a 40% chance, Grid 4 a 60% chance and Grid 5 a 80% chance, compared with the original grid system, giving grid which have greater distortion.

The simulations consider two Reynolds number cases $Re = 100$ and 1000, the length scale was based on the side wall height. Velocities are non-dimensionalized with the lid speed U_{lid}. Pressure is non-dimensionalized by the term ρU_{lid}^2. In the high Reynolds number case, we found that high artificial viscosity is required. Therefore, results are a reflection of not how well non-staggered performs as well as the differencing scheme used.

4.3.1. Low Reynolds number case. Figure 9 shows the predictions of profiles for u-velocity along the centre of the cavity for the fine grid and grids 1, 3 and 5. The predictions using the coarse grids are virtually the same, and we observe that there is very good agreement between

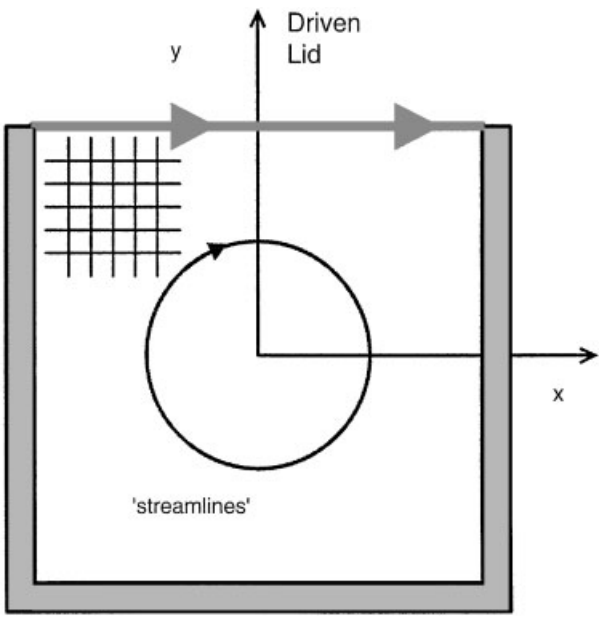

Figure 7. Illustration of the driven-lid problem.

these coarse grid results and the results using the fine grid. The maximum reverse velocity of the coarse grid results is slightly under-predicted relative to the fine grid demonstrating the effect of an increase in artificial viscosity. We observe greater differences in Figure 10, which shows the predictions of the variation of pressure along the central axis of the cavity for the fine grid and grids (1, 3 and 5). There is a greater discrepancy between the fine grid and coarse grid results. The results of all fail to give good agreement with the fine grid near the lower wall. However, the overall profile of these results compared with the results from grid 1 is not greatly dissimilar. The coarse grid results under-predict the overall pressure difference cased by an effective difference in viscosity in the profile, which has been previously observed [12]. An important comment to make about these set of results are there is no high frequency oscillations in the pressure profile (there is no zigzagging or 'wiggles' in the profile). This was an important point to consider when we examined the of pressure contours for the fine grid and grids (1, 3 and 5). The pressure contours show that the fine grid predicts a pressure drop near the top middle of the cavity (although it was off centre it was associated with the recirculation region), as well as four pressure gradients associated with each corner. The top two pressure gradients were, of course, associated with the moving lid and the rapid change in velocity from side-wall to driven lid. The bottom two were associated with the prediction of small recirculation regions in the corners and zero flow regions in the extreme corners. By reviewing other pressure contour for grids 1, 3 and 5 we found that the pattern became distorted. The two dominant pressure gradients changed significantly for the coarse grid and with subsequent distortion. The bottom right-hand corner gradient which had surrounded the bottom and right boundaries started to translate to the right-hand side wall

decreasing in area as the grid became more deformed, on the most deformed grid the pressure gradient decreases dramatically. In comparison to the bottom left pressure gradient it seemed to have merged with the centre and the top left-hand corner pressure gradients. However, the pressure gradients at the top two corners were predicted but were more dispersed compared with the fine grid results. So, with the grids becoming more distorted the contours get more dispersed and the pressure contours translate down the wall and into the centre of the flow near the right-hand boundary. Instead of a distinct pressure drop associated with the centre of the vortex this pressure drop merged with the top left-hand pressure gradient and the bottom left-hand gradient. The pressure contours associated with the more deformed grids appear to give a better representation of the overall pressure field as grids 1 and 3 predict a pressure drop on the right-hand side wall which is not observed in the fine grid set of results. The analysis of the results is confirmed in Table I, which shows the average deviation of the velocity and pressure fields compared with the fine grid results. The grids that are more deformed predict increasing by worse agreement with the fine grid results for the velocity-field, but the change in results is in-significant. However, surprisingly, the more deformed grids predict increasingly better agreement with fine grid results for the pressure-field, though in this case the 'improvement' is very small. We conclude that if we increasingly deform a

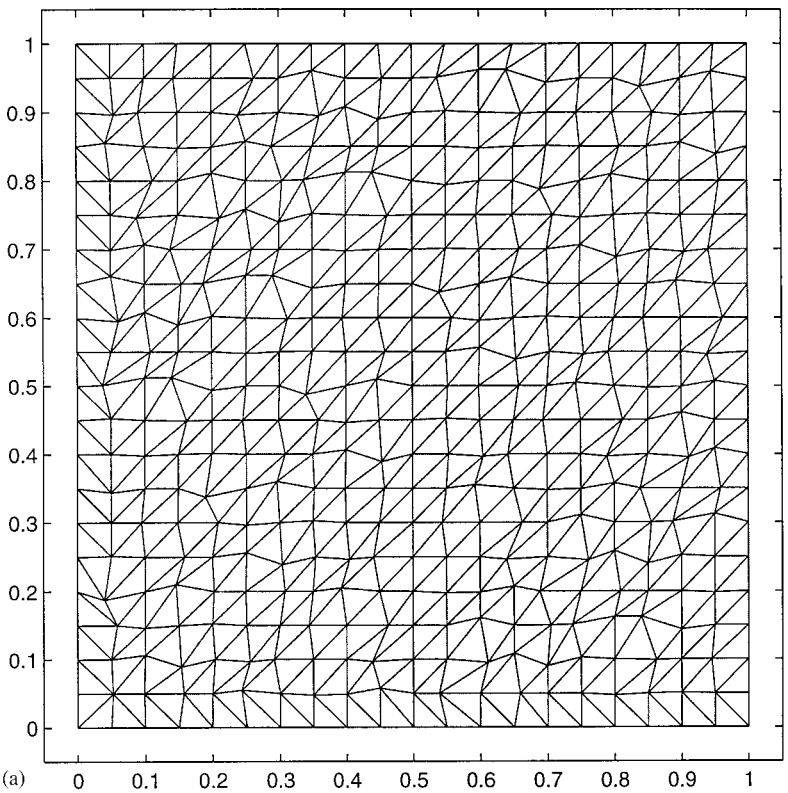

Figure 8. The deformed grids used for the driven-lid problem, (a) grid 3, (b) grid 5.

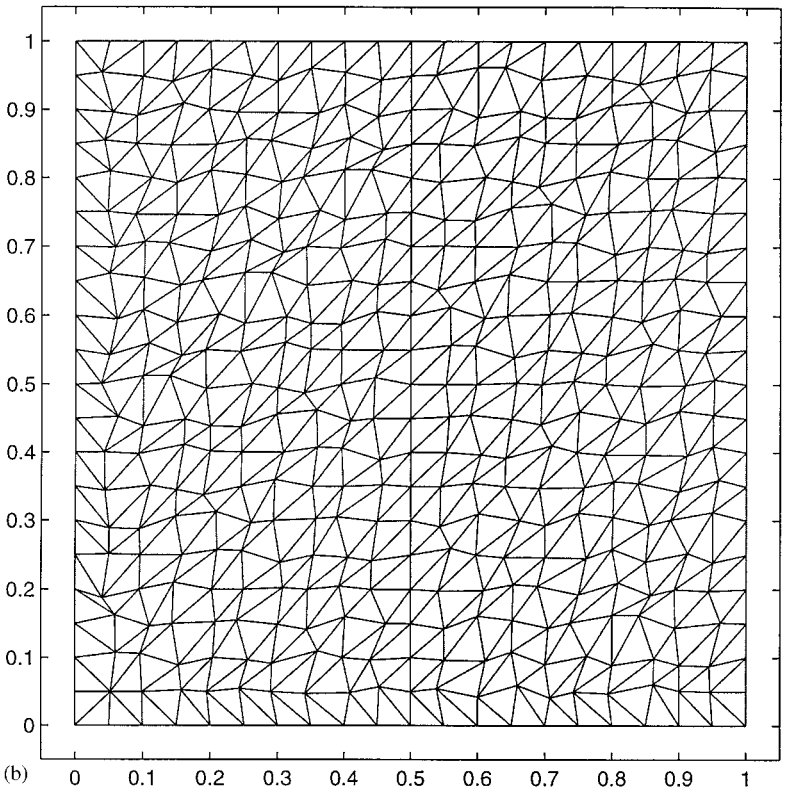

Figure 8. (*Continued*)

regularly spaced grid then the predictions are likely to deteriorate but the deterioration is not significant.

4.3.2. High Reynolds number case. For the high Reynolds number case, we observe that the scheme fails to predict reasonable agreement between the fine grid set of results and the coarse grid set of results. This is due to the differencing scheme being first-order accurate. In Figure 11 there are plots of u-velocity profiles along the centre of the cavity, using the fine grid and the coarse grids (1, 3 and 5). Unlike, the low Reynolds number case, there is a significant degree of disagreement between the various coarse grid results. Grid 1 predicts better agreement with the fine grid set of results, which includes the prediction of a large reverse velocity. Grids 3 and 5 appear to require more artificial viscosity to maintain stability, resulting in worse results. Figure 12 shows the predictions of the variation of the pressure along the central axis of the cavity for the fine grid and grids (1, 3 and 5). The coarse grid results completely fail to predict reasonable agreement with the fine grid results, this is due to the differencing scheme requiring excessive artificial viscosity. Grids 3 and 5 again have worst results than Grid 1. From these profiles it is important to note that there are no pressure-wiggles. The finer grid results, have similar features to its low Reynolds number

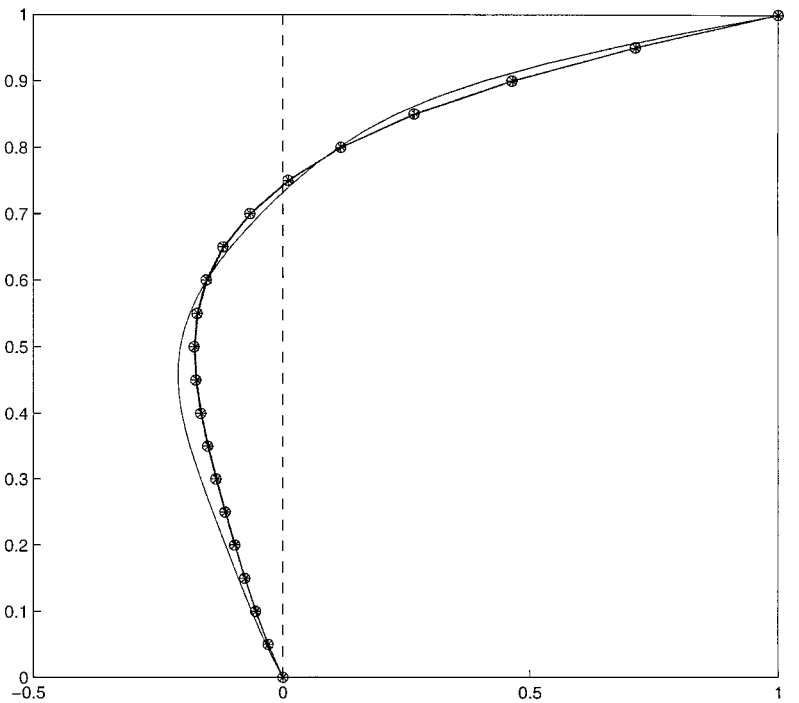

Figure 9. Profiles of the u-velocity along the centre line ($x = 0.5$) of the cavity for $Re = 100$ using the fine grid (continuous line), grid 1 (◯), grid 3 (∅), grid 5 (⊆).

counterpart as discussed earlier. There is a strong pressure gradient at the top right-hand side corner, a pressure drop in the centre of the cavity and at the top left-hand corner there is a strong pressure gradient associated with the corner but there is also another one further along the lid. As with the discussion earlier, there were a number of changes that occurred when we used the coarser grids and increased the distortion. In comparison with the previous study with low Reynolds number, the difference between the coarse grid contours and the fine grid was of a lower magnitude but the general features remain similar. As with previous results the pressure gradients at the bottom disappeared immediately and the bottom left-hand corner did not merge up with the centre. The contours became more dispersed as the distortion increased with the pressure gradients on the top left and right corners tending towards the middle, and the middle pressure gradients transling slightly to the right. These features are successfully predicted using the coarse grids (despite there being no strong qualify agreement). In Table II, we compare the average deviation of field terms u, v and p of the coarse grid results with the fine grid results. The average deviation is found by differences from the course solutions compared with the fourth-order interpolated values from the fine solution, pressure are non-dimensionalized with respect to $1/2\rho U_{\text{lid}}^2$ and velocities with respect to U_{lid}. As we would expect, the values are a lot higher for the velocity terms, though the comparisons for the pressure field have not deteriorated too greatly. Again, the results show a general trend that the more deformed the grid is then the worst the results become, though the deterioration in the results is certainly acceptable in terms of demonstrating a working methodology.

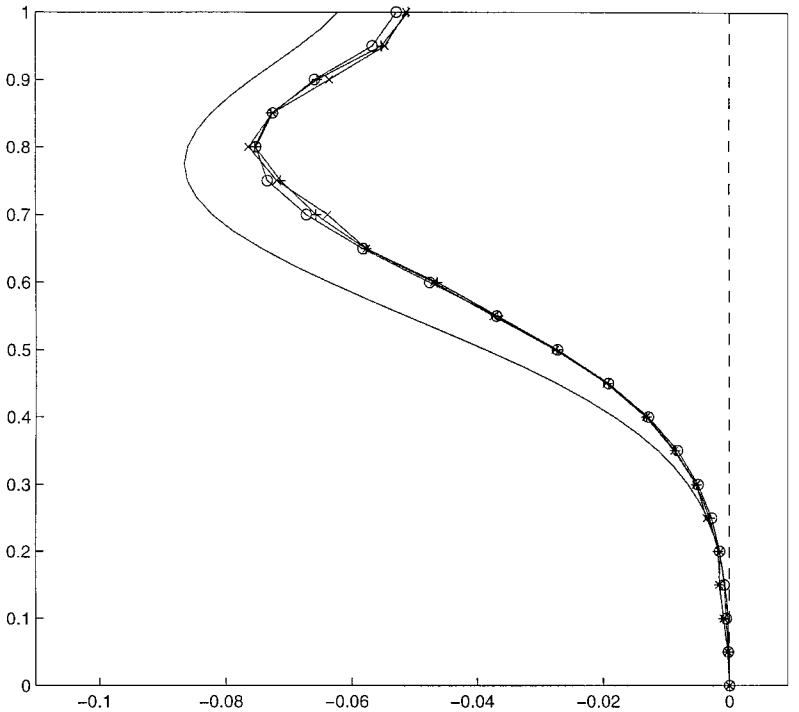

Figure 10. Profiles of the pressure variation along the centre line ($x = 0.5$) of the cavity for $Re = 100$ using the fine grid (continuous line), grid 1 (◯), grid 3 (∅), grid 5 (⊆).

Table I. Calculated average deviations for u, v and p fields between the medium grid results and the fine grid results for $Re = 100$.

	$\sigma(u)$	$\sigma(v)$	$\sigma(p)$
GRID 1	1.81E-2	1.86E-2	2.89E-2
GRID 2	1.87E-2	1.90E-2	2.88E-2
GRID 3	1.90E-2	1.92E-2	2.87E-2
GRID 4	1.92E-2	1.93E-2	2.85E-2
GRID 5	1.96E-2	1.95E-2	2.82E-2

4.4. Flow over a wavy boundary

Flow over a wavy boundary is of interest because there is separation and reattachment caused by the geometry but the positions of separation and reattachment are not fixed. We have predicted a planar laminar flow in a channel which has a lower wavy boundary and a flat upper wall. The flow configuration is illustrated in Figure 13. The geometry has tapered-ends at the inlet and outlet, it is 60 channel-heights long (60 h) and the amplitude of the wavy boundary is 0.4 h. Based on the mean inlet velocity and the inlet channel height, the Reynolds number is $Re = 800$. A parabola streamwise velocity profile is prescribed at the inlet and

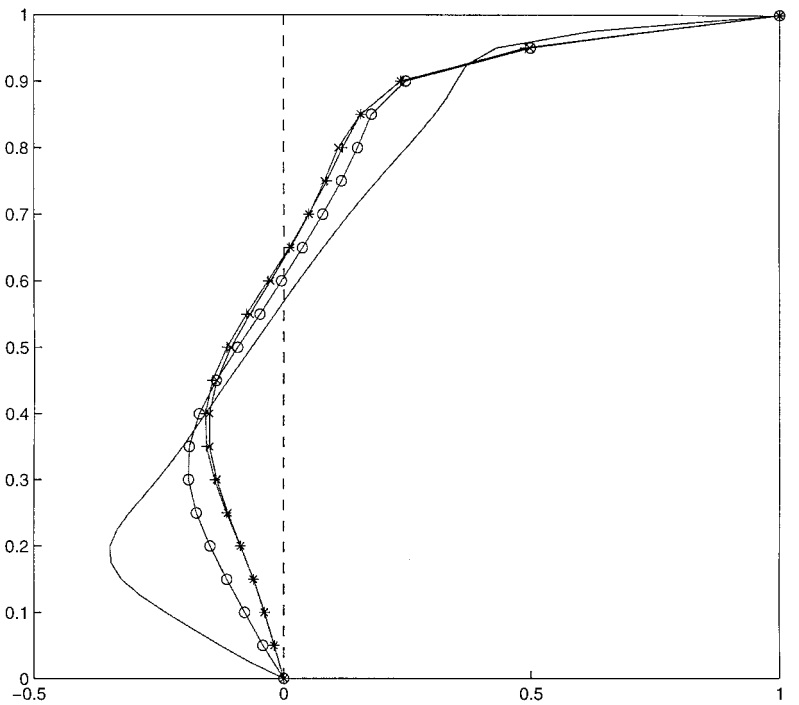

Figure 11. Profiles of the u-velocity along the centre line ($x = 0.5$) of the cavity for $Re = 1000$ using the fine grid (continuous line), grid 1 (◯), grid 3 (∅), grid 5 (⊆).

first-order extrapolation is applied at the outlet. No-slip boundary conditions are applied at all the walls and pressure extrapolation is applied for the boundaries.

The grid for the simulation uses 130×80 points. The grid is stretched and compressed in the vertical direction in order to achieve the wavy effect. The complete grid system and a section of the grid in the mid-range $x = -1 - 11$ is shown in Figure 14. We show u-velocity profiles for this mid-section of the channel, in Figure 15. The profiles in the first trough are slightly different to those in the second trough because the positions of the profiles are slightly out-of-phrase with each other. Nevertheless, the figure does illustrate the fact that the flow is virtually periodic. The simulation predicts separation occurring just after a peak and it reattaches at a similar location on the opposite wall. The flow rapidly decelerates, as it enters a trough. A contour plot of the pressure field for the mid-section is shown in Figure 16. The pressure field reflects the behaviour of the velocity field, there is an adverse pressure gradient associated with the separation point and a pressure rise associated with the reattachment. As the flow leaves a trough there are strong pressure gradients reacting against the sudden constriction of flow, when the flow enters a new trough we observe rapid pressure recovery. We can observe the periodic behaviour of the flow by plotting the maximum streamwise velocity against distance in Figure 17. The figure shows how the maximum streamwise velocity rises and falls in phase with the wavy boundary, there is a slight gradual rise in the maximum streamwise velocity with distance as the flow is pushed away from the lower boundary with each peak it passes over.

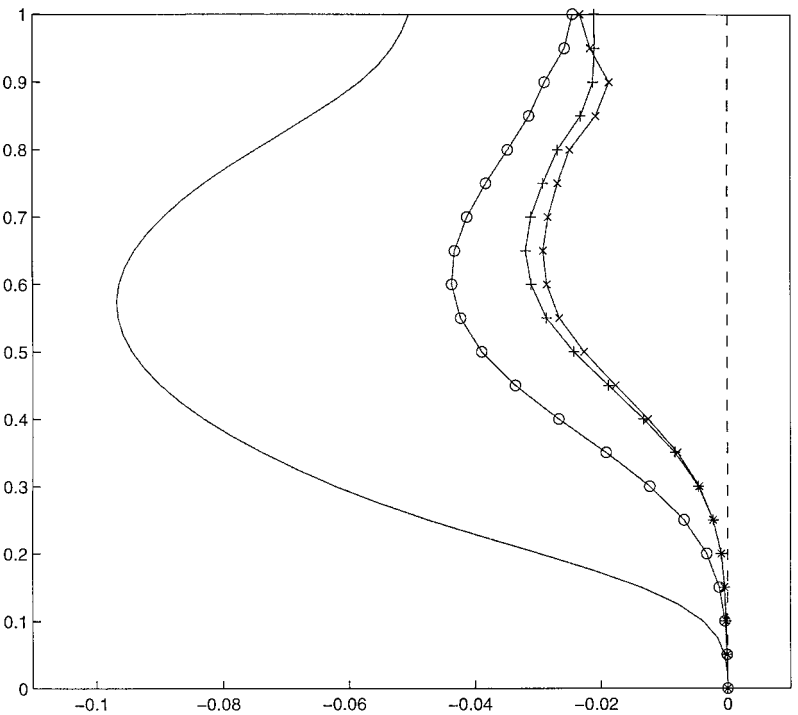

Figure 12. Profiles of the pressure variation along the centre line ($x = 0.5$) of the cavity for $Re = 1000$ using the fine grid (continuous line), grid 1 (◯), grid 3 (∅), grid 5 (⊆).

Table II. Calculated average deviations for u, v and p fields between the medium grid results and the fine grid results for $Re = 1000$.

	$\sigma(u)$	$\sigma(v)$	$\sigma(p)$
GRID 1	5.12E-2	5.27E-2	2.93E-2
GRID 2	5.77E-2	6.22E-2	3.19E-2
GRID 3	6.67E-2	6.84E-2	3.33E-2
GRID 4	6.60E-2	6.95E-2	3.34E-2
GRID 5	6.58E-2	6.98E-2	3.38E-2

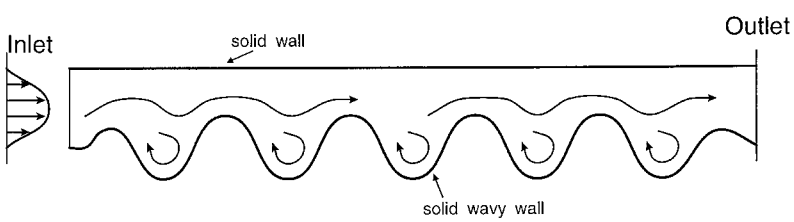

Figure 13. Illustration of the 'laminar flow over a wavy boundary' problem.

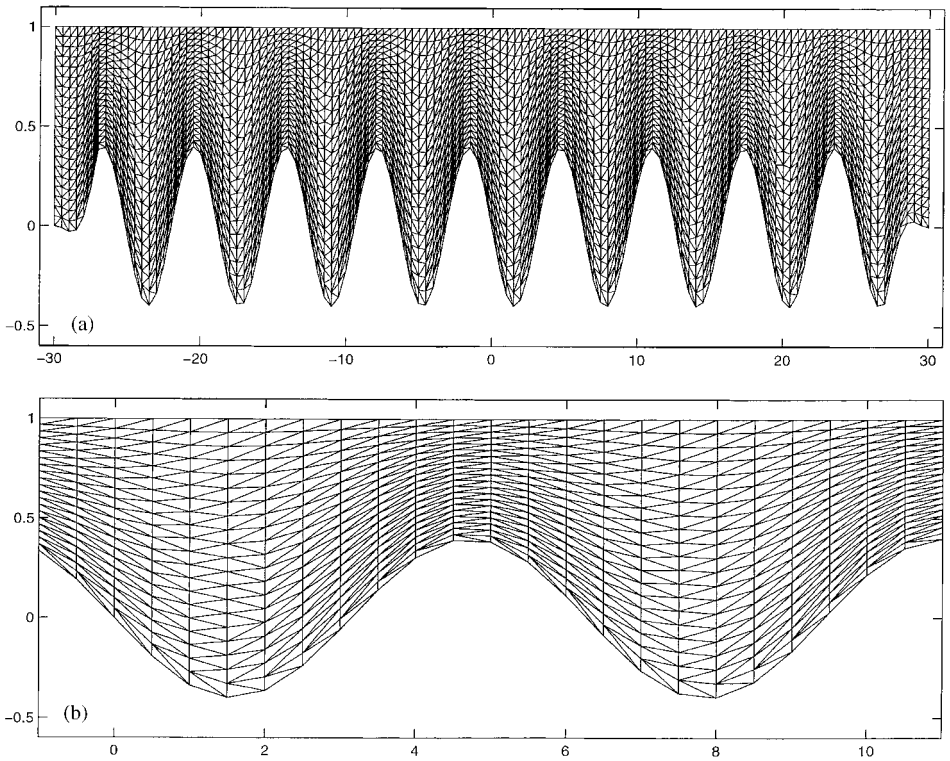

Figure 14. The grid system used for the wavy boundary problem (a) the complete grid system, (b) a section of the grid between $x = -1$ to 11.

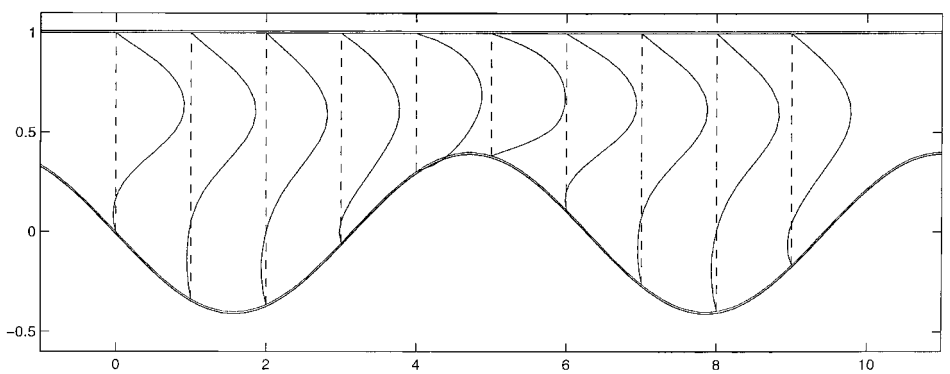

Figure 15. Profiles of the u-velocity at various locations in the range $x = -1$ to 11.

5. CONCLUDING REMARKS

We have developed a non-staggered methodology which uses a pressure dissipation term in order to suppress wiggles in the pressure field. The development allows us now to apply

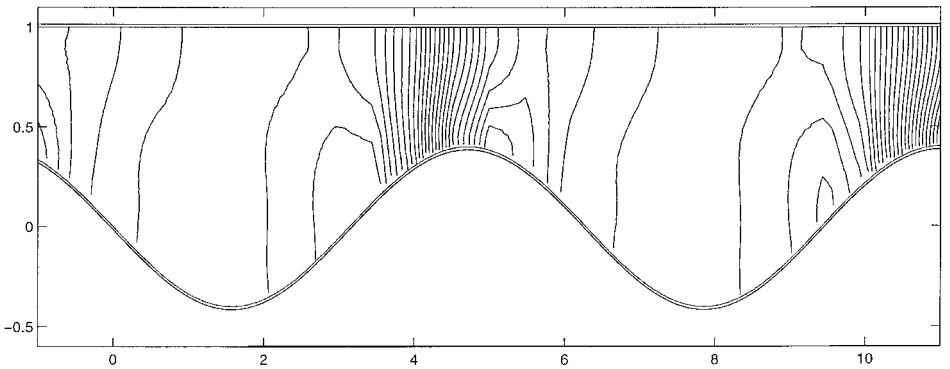

Figure 16. A contour plot of the pressure field in the range $x = -1$ to 11.

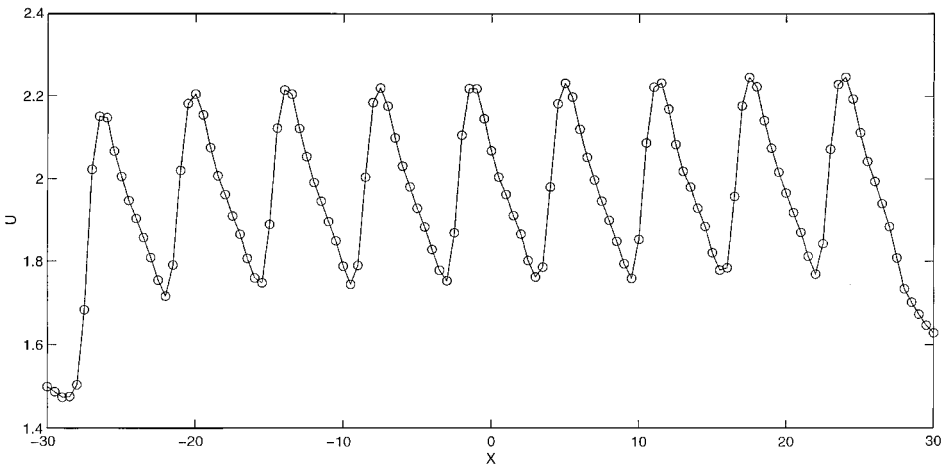

Figure 17. The variation of maximum predicted streamwise velocity with distance from inlet to the outlet.

the scheme to unstructured grid systems. Standard finite volume methodology is used for discretization.

The comparisons of the flow over a cylinder and the flow over a backward facing step between the standard finite volume solver and the new methodology show a good agreement. Flow simulations for the backward facing step had insignificant differences. Although the results for the flow over a cylinder problem are not identical, these results further established the validity of the new non-staggered methodology finite volume solver. Grid refinement tests shown with the backward facing step show that the new differencing scheme is very sensitive to refinement in the grid. The sensitivity is not surprising as the scheme is based on central differencing terms and does not successfully introduce the hyperbolic nature of the flow. But it works with sufficient grid refinement. From our experience we do not recommend using this approach for a finite volume or meshless method unless the practitioner is prepared to

use a fine grid and wants to develop a solver where the spatial functions are calculated once at the beginning.

The new non-staggered methodology was further investigated using the standard 'driven-lid' problem. In the test increasingly deformed grid structures were used to predict the flow. It was found that by increasing the deformation of the grid the agreement with fine grid results deteriorated, as we would expect, though the deterioration was not excessive. The deterioration of the results was found to be strongly effected by the differencing scheme for the high Reynolds case.

In conclusion, the non-staggered methodology is successful but a better differencing scheme needs to be developed to deal with coarse grid distributions. We have also demonstrated that the scheme can be used to predict more complex flows with stretching and distortion of the control volumes.

ACKNOWLEDGEMENTS

Thanks are due to Mr Barry Jaber and Mr Phil Athayde, for conversions and insights that have contributed to the development of this paper.

REFERENCES

1. Bressloff NW. A parallel PISO algorithm applied to flow at all speeds. *International Journal for Numerical Methods in Fluids* 2001; **36**:497–518.
2. Markham-Smith D, Barton IE. The solution of convection–diffusion problems with the use of meshless structured grid systems. *ECCOMAS Barcelona* 2000.
3. Patankar SV. *Numerical Heat Transfer and Fluid Flow*. Hemisphere: Washington DC, 1980.
4. Rhie CM, Chow WL. Numerical study of the turbulent flow past an airfoil with trailing edge separation. *AIAA Journal* 1983; **21**:1525–1532.
5. Coelho PJ, Pereira JCF. Finite volume computation of the turbulent-flow over a hill employing 2D or 3D non-orthogonal collocated grid systems. *International Journal for Numerical Methods in Fluids* 1992; **14**: 423–441.
6. Kobayashi MH, Pereira JCF, Sousa JMM. Comparison of several open boundary numerical treatments for laminar recirculating flows. *International Journal for Numerical Methods in Fluids* 1993; **16**:403–419.
7. Lai CJ, Yen CW. Turbulent free-surface flow simulation using a multilayer model. *International Journal for Numerical Methods in Fluids* 1993; **16**:1007–1025.
8. Cheng L, Armfield S. A simplified marker and cell method for unsteady flows on non-staggered grids. *International Journal for Numerical Methods in Fluids* 1995; **21**:15–34.
9. Armfield SW. Finite difference solutions of the Navier–Stokes equations on non-staggered grids. *Computers Fluids* 1991; **20**:1–17.
10. Armfield SW. Fourth order elliptic correction for the Navier–Stokes equations on non-staggered grids. In *Computational Techniques and Applications Conference*, *CTAC-95*. May RL, Easton AK (eds). World Scientific: Singapore, 1996; 113–119.
11. Barton IE. Improved laminar predictions using a stabilised time dependent simple scheme. *International Journal for Numerical Methods in Fluids* 1998 28; **5**:841–857.
12. Barton IE, Kirby R. Finite difference scheme for the solution of fluid flow on unstructured non-staggered grids. *International Journal for Numerical Methods in Fluids* 2000; **33**:939–959.
13. Majumdar S. Role of under-relaxation in momentum interpolation for calculation of flow with non-staggered grids. *Numerical Heat Transfer* 1998; **13**:125–132.
14. Miller TF, Schmidt FW. Use of a pressure-weighted interpolation method for the solution of incompressible Navier–Stokes equations on a non-staggered grid system. *Numerical Heat Transfer* 1988; **14**:213–233.
15. Schonauer W, Adolph T. The FDEM (Finite Difference Element Method) program package: fully parallelized solution of elliptic and parabolic PDEs. *ECCOMAS Barcelona* 2000.
16. Anderson DA, Tannehill JC, Pletcher RH. *Computational Fluid Mechanics and Heat Transfer*. Hemisphere: Washington, DC, 1984.
17. Thakur, S, Wright J, Shyy W. A pressure-based composite method with conservative interface treatment. *AIAA 96-0298*. 1996.

18. Van Doormaal, JP, Raithby GD. Enhancements of the SIMPLE method for predicting incompressible fluid flows. *Numerical Heat Transfer* 1984; **7**:147–163.
19. Darwish MS. A new high-resolution scheme based on the normalized variable formulation. *Numerical Heat Transfer Part B* 1993; **24**:353–371.
20. Van Leer B. Towards the ultimate conservative difference scheme. II. Monotonicity and conservation combined in a second order scheme. *Journal of Computational Physics* 1974; **14**:361–370.
21. Melaaen MC. Analysis of fluid-flow in constricted tubes and ducts using body-fitted nonstaggered grids. *International Journal for Numerical Methods in Fluids* 1992; **15**:895–923.
22. Melaaen MC. Calculation of fluid flows with staggered and nonstaggered curvilinear nonorthogonal grids—the theory. *Numerical Heat Transfer Part B* 1992; **21**:1–19.
23. Barton IE. Laminar flow past an enclosed and open backward-facing step. *Physics of Fluids* 1994; **6**(12): 4054–4056.
24. Armaly BF, Durst F, Pererira JCF, Schonung B. Experimental and theoretical investigation of backward-facing step. *Journal of Fluid Mechanics* 1983; **127**:473–496.
25. Barton IE. A numerical study of flow over a confined backward facing step. *International Journal for Numerical Methods in Fluids* 1995; **21**:653–665.
26. Kim J, Moin P. Application of a fractional-step method to incompressible Navier–Stokes equations. *Journal of Computational Physics* 1985; **59**(2):308–323.
27. Orlandi P. Vorticity velocity formulation for high Re flows. *Computer & Fluids* 1987; **15**(2):137–149.
28. Thangam S, Knight DD. A computational scheme in the generalised co-ordinates for viscous incompressible flow. *Computer & Fluids* 1990; **18**(4):317–327.
29. Thangam S, Knight DD. Effect of height step on the separated flow past a backward facing step. *Physics of Fluids A* 1989; **1**(3):606–606.
30. Chiang TP, Shue TWH. Vortical flow over a 3-D backward facing step. *Numerical Heat Transfer Part A* 1997; **31**(2):167–192.
31. Caruso SC, Ferziger JH, Oliger Journal Adaptive grid techniques for elliptic fluid flow problems. *AIAA 24th Aerospace Science Meeting. Paper no. AIAA-86-0498*, Reno, Nevada 1986.
32. Hetu JF, Pelletier DH. Fast adaptive finite element scheme for viscous incompressible flows. *AIAA Journal* 1992; **30**(11):2677–2682.
33. Gartling DK. A test problem for outflow boundary conditions—flow over a backward facing step. *International Journal for Numerical Methods in Fluids* 1990; **11**(7):953–967.
34. Harms TM, von Backstrom TW, du Plessis JP. Reformation of the SIMPLEN discretization scheme to accommodate non-centralized interfaces. *Numerical Heat Transfer B* 1991; **20**:127–144.
35. Date AW. Solution of Navier–Stokes equations on non-staggered grids. *International Journal of Heat and Mass Transfer* 1993; **36**:1913–1922.
36. Lee SL, Tzong RY. Artificial pressure for pressure-linked equation. *International Journal of Heat and Mass Transfer* 1992; **35**:2705–2716.

